Vol. 6 • No. 8 • August • 2021

www.advmattechnol.com

ADVANCED MATERIALS TECHNOLOGIES

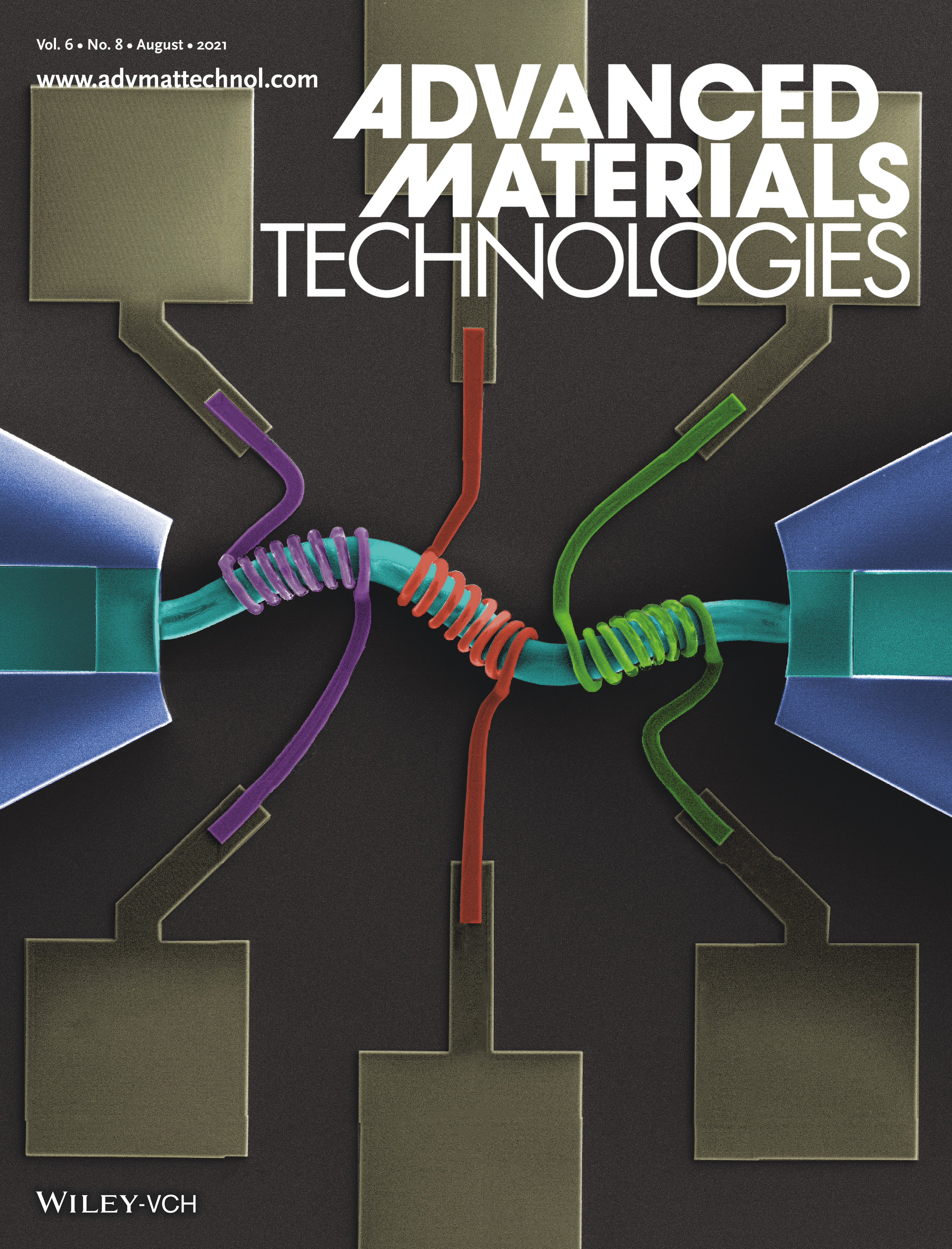

WILEY-VCH

In Situ Direct Laser Writing of 3D Graphene-Laden Microstructures

*Michael Restaino, Noah Eckman, Abdullah T. Alsharhan, Andrew C. Lamont, Jackson Anderson, Dana Weinstein, Asha Hall, and Ryan D. Sochol**

A wide range of applications rely on the ability to integrate electrically conductive microstructures with microfluidic channels. To bypass the planar geometric restrictions of conventional microfabrication processes, researchers have recently explored the use of "Direct Laser Writing (DLW)"—a submicron-scale additive manufacturing (or "3D printing") technology—for creating conductive microfeatures with fully 3D configurations. Despite considerable progress in the development of DLW-compatible photomaterials, thermal post-processing requirements to support electrical conductivity remain a critical barrier to microfluidics integration. In this work, novel graphene-laden photocomposites are investigated to enable DLW-based printing of true 3D conductive microstructures directly inside of enclosed microchannels (i.e., in situ). Photoreactive composite materials comprising reduced graphene oxide (rGO) particle concentrations of up to 10 wt% exhibited high compatibility with DLW, with minimal optical interference at critical wavelengths. Developed rGO-photocomposites revealed an ultimate DC conductivity of 9.85 ± 0.48 × 10^{-5} S m^{-1}. Experimental results for DLW of 3D microcoils (1 wt% rGO; wire diameter = 10 µm; coil diameter = 40 µm) revealed an impedance of 2.71 ± 0.12 MΩ at 2 MHz. In addition, results for in situ DLW of geometrically sophisticated rGO-laden microstructures suggest utility of the presented approach for potential 3D microelectronics-based microfluidic applications.

Microfluidic systems with integrated electronics have widespread applications in chemical[1–3] and biological[4–6] sensing, fluidic manipulation,[7] and nanoparticle processing.[8] Historically, methods of integrating electrically conductive materials with microfluidic systems have relied primarily on conventional clean room-based microfabrication processes, which often impose geometric limitations with respect to device design.[9] Although researchers have developed approaches to circumvent these restrictions and achieve more 3D device architectures, such methods necessitate exceedingly time-consuming and labor-intensive protocols.[10] Consequently, researchers have increasingly begun investigating the use of additive manufacturing (or colloquially, "3D printing") technologies as a promising alternative.[11] Despite the material selection benefits associated with extrusion-based approaches (e.g., direct ink writing), the physical restrictions inherent to nozzle-mediated deposition represent a critical impediment to integration with microfluidic channels.[12] In

---

M. Restaino, Dr. A. T. Alsharhan, Prof. R. D. Sochol
Department of Mechanical Engineering
University of Maryland
College Park, MD 20742, USA
E-mail: rsochol@umd.edu

M. Restaino, Prof. R. D. Sochol
Fischell Department of Bioengineering
University of Maryland
College Park, MD 20742, USA

N. Eckman
Department of Chemical and Biomolecular Engineering
University of Maryland
College Park, MD 20742, USA

Dr. A. T. Alsharhan
Department of Mechanical Engineering
Kuwait University
Safat 13060, Kuwait

The ORCID identification number(s) for the author(s) of this article can be found under https://doi.org/10.1002/admt.202100222.

DOI: 10.1002/admt.202100222

Dr. A. C. Lamont
Division of Biomedical Physics
Office of Science and Engineering Laboratories
Center for Devices and Radiological Health
U.S. Food and Drug Administration
Silver Spring, MD 20993, USA

J. Anderson, Prof. D. Weinstein
Department of Electrical and Computer Engineering
Purdue University
West Lafayette, IN 47907, USA

Dr. A. Hall
United States Army Research Laboratory
Aberdeen Proving Grounds
Aberdeen Proving Ground, MD 21005, USA

Prof. R. D. Sochol
Robert E. Fischell Institute for Biomedical Devices
University of Maryland
College Park, MD 20742, USA

Prof. R. D. Sochol
Maryland Robotics Center
University of Maryland
College Park, MD 20742, USA

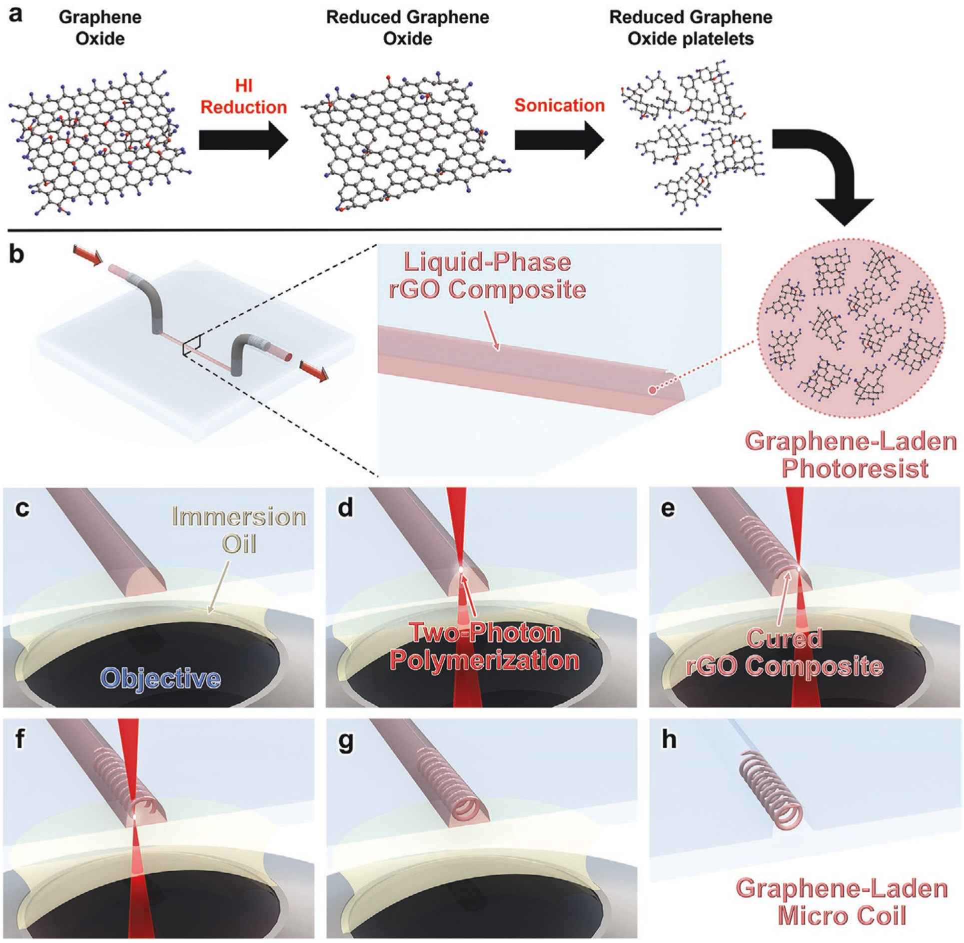

Figure 1. Conceptual overview of manufacturing 3D graphene-laden photocomposite and resultant structures inside microfluidic channels via *is*DLW. a) Conversion pathway of insulative graphene oxide (GO) into conductive rGO platelets. b) Loading of liquid-phase graphene-laden photoresist into a COP microdevice. c–h) *Is*DLW fabrication. c) Loaded microdevice in the oil-immersion printing mode. d–f) "Ceiling-to-floor", point-by-point, layer-by-layer two-photon (or multi-photon) polymerization via a focused, pulsed IR laser. g) Fully printed and developed 3D graphene-laden micro coil inside of an enclosed microchannel.

contrast, the submicron-scale 3D manufacturing technique, "Direct Laser Writing (DLW)", allows for geometrically complex microstuctures to be printed directly inside of enclosed microchannels—a strategy termed "in situ DLW (*is*DLW)".[13]

DLW uses tightly focused femtosecond IR laser pulses to initiate spatially controlled photopolymerization via two-photon (or multi-photon) absorption phenomena.[14] This approach can be automated to precisely crosslink (i.e., solidify) a liquid-phase, photocurable material at designated locations in a point-by-point, layer-by-layer manner to produce 3D objects comprising cured polymeric materials with resolutions on the order of 100 nm.[15] Previously, researchers have developed a wide array of DLW-compatible photocomposites containing electrically conductive filler components, such as single and multi-wall carbon nanotubes (CNT)[16] as well as nickel,[17] silver,[18] silver nanowires,[19] and gold nanoparticles.[20,21] Previous works demonstrating DLW-fabricated, conductive composite structures employed thermal post-processing treatments (e.g., pyrolysis) at high temperatures to remove or reduce the highly resistive polymer matrix and to produce a suitably conductive structure.[22] Because the temperatures needed to reduce the polymeric matrix (e.g., di- or triacrylic-based polymers) are greater than 350 °C,[23] however, such approaches are incompatible with standard microfluidic device materials, such as poly(dimethylsiloxane) (PDMS) or thermoplastics.

Since the first discovery of graphene, various forms of graphene-based composites have been formulated to take advantage of its superb electrical conductivity.[24] In particular, few-sheet graphene fillers are well suited for DLW composites as they have been shown to have high optical transmittance (>90%) and electron mobility.[25] Unlike other carbon-based composite fillers such as CNTs, the impact of dispersion restrictive behaviors is strongly reduced in graphene-based composites. Due to the 2D nature of graphene, the particles are permitted to slide over each other in shear enabling composites with a filler content of up to approximately 20 wt%.[26] In this work, we explore a strategy for the creation and integration of a novel DLW-compatible graphene-laden photocomposite that is uniquely suited for the fabrication of 3D microstructures directly inside of enclosed microfluidic channels (**Figure 1**). We investigate the compatibility of particle processing times as

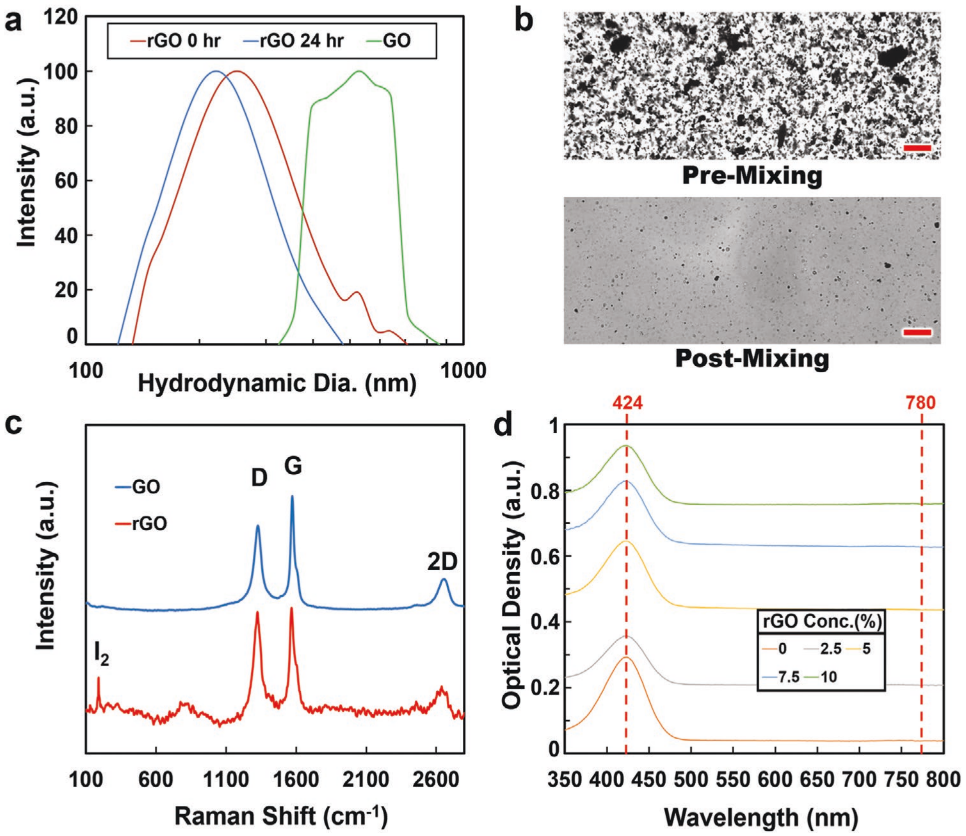

Figure 2. Optical characterization of the synthesized rGO and rGO photocomposite. a) DLS results showing the size reduction that occurs when GO is reduced to rGO and the effects of sonication of rGO over 24 h. b) Brightfield micrograph of the incorporation of rGO particles into the photoresist before and after mixing. Scale bars = 50 µm. c) Raman spectra analysis of GO and rGO. d) Optical density results of IP-Dip photopolymer and varying concentrations of rGO.

well as graphene concentrations in the composite and the corresponding optical impact. Lastly, we investigate the electrical performance of DLW-printed graphene-laden microstructures through impedance analysis. The presented composite and results serve as a critical baseline in demonstrating that DLW can be employed as a versatile strategy to print complex and conductive 3D graphene-laden microstructures embedded directly within microfluidic channels.

The graphene-laden photoresist in this work contains conductive rGO nanoplatelets produced via a previously established protocol (Figure 1a) in which GO is chemically reduced by HI while under mechanical agitation.[25] Due to the removal of GO's oxygen functional groups, the rigorous mixing involved and a post-reduction ultra-sonication step, there was an associated decrease in overall particle/platelet sheet size. Dynamic light scattering (DLS), an emerging facile, quick, and reliable method to characterize nanosheets in situ, was used to quantify the size reduction of the rGO nanoplatelets. Although there is a large amount of uncertainty in the lateral size measurement, DLS has been found to be useful for comparing significant differences in nanosheet size.[27] The mean hydrodynamic diameter (d_{hd}) attained from DLS can be approximated as the diameter of a sphere with volume equal to the mean GO/rGO sheet volume. The d_{hd} was measured before and after the processing of GO to rGO, **Figure 2**a, and a roughly 40% shift in the average particle's d_{hd} was observed with the d_{hd} of both GO and rGO found to be 478 ± 9 to 285 ± 3 nm, respectively. An additional test was conducted after 24 h of sonication to observe any particle size effects that the sonication time utilized in the dispersion of the rGO in the photopolymer would have on the nanoplatelets (Figure 2b). The resulting nanoplatelets were found to have a further reduction of roughly 8.7% transitioning from a d_{hd} of 285 ± 3 to 260.5 ± 5 nm.

Raman Spectroscopy was used to assess the degree of defects present in the GO and rGO sheets (Figure 2c). Graphene's Raman spectra are generally characterized by the presence of both the D (1350 cm^{-1}) and G (1583 cm^{-1}) band peaks associated with graphitic materials. In addition, a 2D band (2635 cm^{-1}) was observed, which is often associated with the oxidation of the graphene sheets. From the intensities of the D and G band of the spectra, an I_D/I_G ratio—commonly used to determine the evolution of defects as a result of the reduction process—of 0.92 was observed, which was distinct from the GO's I_D/I_G ratio of 0.69. The increase of the I_D/I_G ratio from the untreated GO to rGO is consistent with prior results reported by other groups for HI-rGO reductions.[25] In addition, a small but prominent peak was observed at 190 cm^{-1} alluding to the presence of iodine residuals from the reduction process as the peak's location is within iodine's known vibrational mode range on few-layer graphene sheets of 103–203 cm^{-1} (Figure 2c).[28] Raman

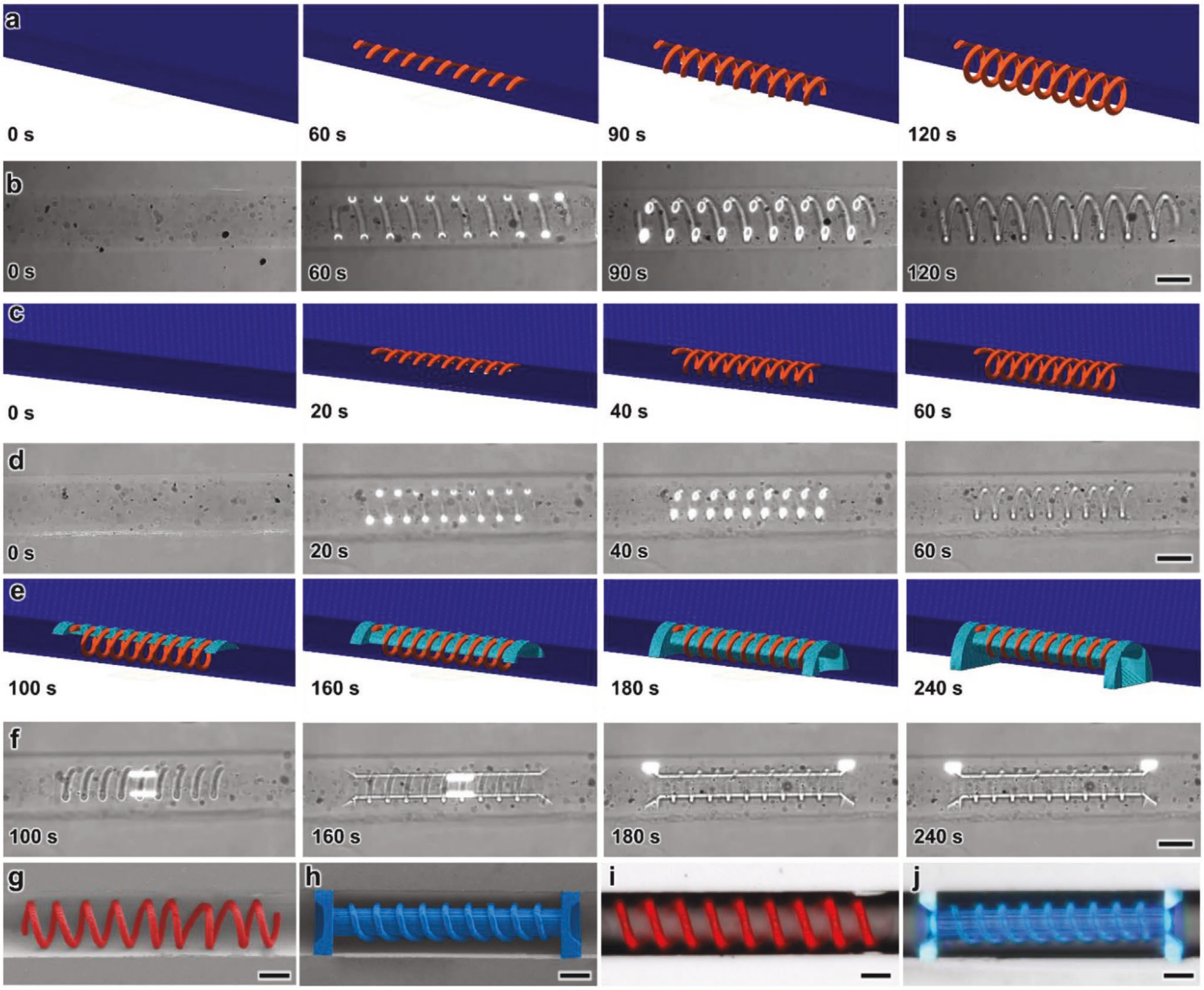

Figure 3. DLW fabrication results. Sequential frames from video of a) CAM simulation of the DLW fabrication process and b) DLW printing of a 3D graphene-laden microcoil. Sequential frames from video of d,f) CAM simulation of the multi-component DLW fabrication process and c,e) DLW printing of a 3D graphene-laden microcoil-wrapped channel. g,h) False-colored scanning electron and i,j) fluorescent micrographs of the DLW printed microcoil and microcoil-wrapped channel composite structures. (Scale Bar = 20 µm).

spectral analysis of a single photon cured sample of the developed rGO composite (Figure S2, Supporting Information) was attempted, however, the intense autofluorescence of IP-Dip at the available Raman source lasers (532 and 633 nm) blocked out any contributing signal from the graphene nanoparticles, impeding interfacial and chemical structural analysis.

To evaluate the compatibility of the designed rGO particles with the DLW printing process, optical density testing was conducted on various rGO composites. Particle concentrations ranging from 0 to 10 wt% were analyzed over 350–800 nm. IP-Dip's optical density maxima were found to be at 424 nm and can be associated with IP-Dip's photoinitiator peak activation, therefore, any deviations or shifting of the maxima in the rGO composite serves to reduce the photoinitiator's ability to produce free radicals and, in turn, the polymerization of the photoresist into the intended 3D structures. The optical density testing of photocomposites with up to 10 wt% rGO revealed that although the optical density increased with increasing rGO concentration, the general absorption behavior was maintained (<1% deviation at 424 nm) (Figure 2c). Similarly, the optical density of the rGO composites at 780 nm—the operating wavelength of the 3D printer's laser—increased with the increase of rGO concentration without the addition of any local maxima or minima. The optical behavior of the composites at both 424 and 780 nm confirms that, even with large concentrations of rGO particles, no unexpected scattering phenomena occur. It was also observed that with rGO concentrations greater than 1 wt%, the effective dose range required to successfully polymerize the composite increased. We believe this increase is not solely due to a rise in the scattering caused by the rGO nanoplatelets, but also rGO's ability to act as a free radical scavenger.

To demonstrate the fabrication of the rGO-laden photocomposite with *is*DLW, an 8-turn, 5 µm thick microcoil with an inner diameter of 20 µm was printed inside of a 30 µm tall and 40 µm wide

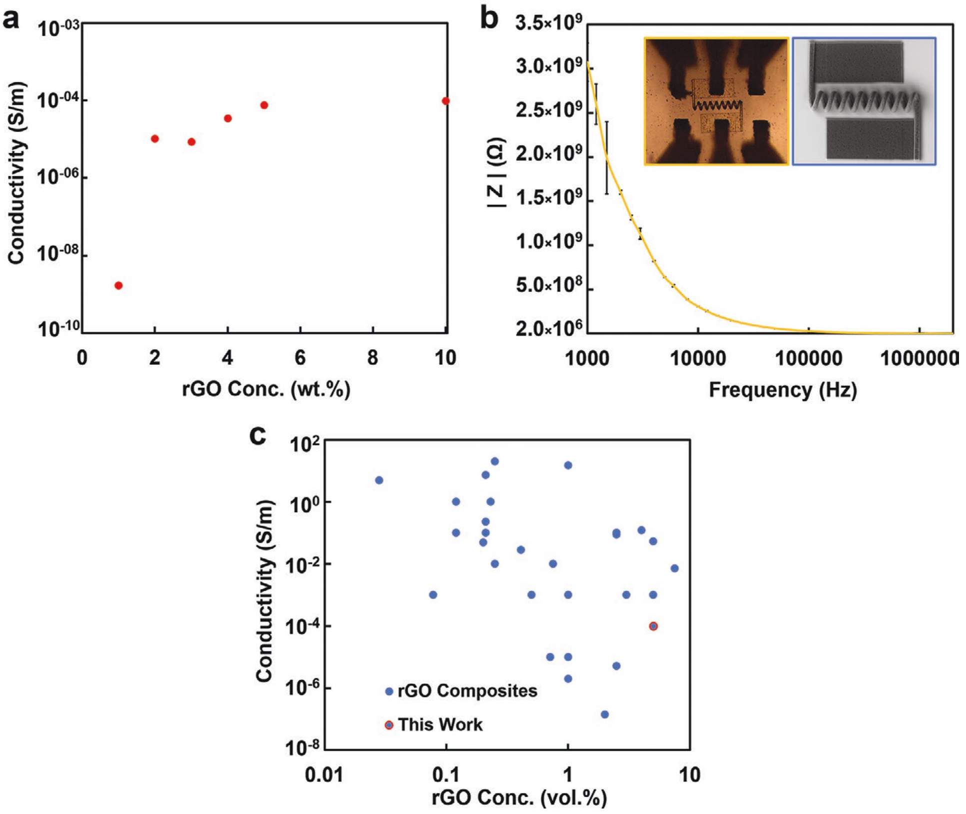

Figure 4. Electrical performance results of the developed graphene-laden photocomposite. a) Conductivity measurements of graphene-laden thin films. b) Impedance analysis of an 8-turn microcoil (inset image). c) Comparison of the graphene-laden composite designed in this work against similarly reported graphene composites.[40]

enclosed microfluidic channel. Computer-aided manufacturing (CAM) software was utilized to convert and simulate a 3D microcoil model into the writing-path code that governs the positioning of the printing laser's focal point during the fabrication process. Sequential frames of the CAM simulations and the corresponding printing video frames are presented in **Figure 3**a,b, respectively.

Due to the nature of rGO nanoparticles and their affinity for aggregation, large agglomerates were present in the photocomposite during the printing of the microcoils; however, the impact on the printing process was substantially reduced by maintaining the printing exposure dose, estimated as being proportional to the square of the laser power over the scan speed, roughly equal to 0.036. At this relative exposure dosage, even the larger of these aggregates produced limited bubbling and/or no burning effects and were observed to have no noticeable impact on the structures while printing. To investigate the compatibility of the developed photocomposite with more complex, multi-component structures, an 8-turn microcoil-wrapped channel was sequentially fabricated by first printing a microcoil bound to the ceiling of the microfluidic channel and subsequently printing a hollow fluidic channel through the microcoil's center. Sequential frames of the CAM simulations of the multi-component print and the corresponding printing video during the printing process are presented in Figure 3c–f. A complete side-by-side video of both in-channel prints and CAM simulations can be seen in their entirety in the provided supplementary materials (Movie S1 and S2, Supporting Information). After the printing process was complete, the temporarily bonded thin cyclic olefin polymer (COP) base sheet was removed, and the top section of the microfluidic device containing the embedded printed structures was developed and then imaged via a fluorescent microscope and a scanning electron microscope (SEM). Both fluorescent and false-colored SEM micrographs of the resulting printed microcoil and microcoil-wrapped channel can be seen in Figure 3g–j.

The bulk material electrical performance of the rGO photocomposite was studied through thin film analysis. Single photon, UV-cured thin film samples of the synthesized rGO photocomposite were created using a UV lamp and tested with a four-point resistivity system to measure the sheet and bulk resistance. The resulting conductivities of the thin film samples (**Figure 4**a) revealed an ultimate DC conductivity of 9.85×10^{-5} (S m^{-1}) with an rGO loading of 10 wt%. The developed photocomposite's percolation threshold and associated conductive behavior followed that of previously published work with carbon-based filler particles in polymer composites (e.g., Pott et al. with rGO and natural rubber nanocomposites).[29,30]

In addition to being a useful method of characterizing the electrical performance of composite materials,[31] impedance spectroscopy is a common technique used in microfluidic devices with integrated microelectronics designed for biological analysis such as cell or bacterial detection,[32] particle detection,[33] and chemical sensing.[34] To investigate the AC performance of the microstructures fabricated with the developed photocomposite, an 8-turn microcoil printed between two patterned ITO contact pads was printed (Movie S3, Supporting Information), with an rGO particle loading of 1 wt%. The impedance analysis of the printed microstructure was conducted over a frequency range of 1 kHz to 2 MHz (Figure 4b). The tested microcoil was found to exhibit a strong frequency-dependent AC resistance, which is believed to be due to the non-ohmic resistances associated with polymer composite films at frequencies below <10 MHz.[31,35] Similar frequency-dependent impedances have been observed in polymer composites with carbon-based conductive filler components.[36–38] Comparing the fabricated microcoil's impedance behavior to these previously studied polymer composite films suggests that at the 1 wt% rGO particle loading, the electrical performance is driven mainly by the material properties instead of geometry. The impedance testing of the DLW-printed microcoil, seen in the inset micrograph in Figure 4b, was found to exhibit a comparable signal to that of previous quasi-3D DLW-printed conductive structures. More specifically, the AC response of the microcoil was similar to that of work by Vaithilingam et al., who conducted impedance testing on a quasi-3D DLW printed structure composed of a multiwalled carbon nanotube photocomposite and was subsequently utilized to successfully electrically stimulate human-induced stem cell-derived cardiomyocytes.[39] The similar performance of these two works serves to demonstrate the potential uses of the developed graphene-laden photocomposite for bio-based microfluidic applications.

It is important to note the electrical conductivity shown in Figure 4a is from the analysis of single-photon cured thin films of the rGO composite. Figure 4a is intended to observe the conductivity of the composite without any confounding variables introduced during the DLW printing process that was not directly investigated in this work (e.g., layer slicing, hatching, orientation, laser power, and scanning speed). Prior work such as that by Ushiba et al. demonstrated the impact of DLW printing parameters by showing the path and polarity of the laser can be used in the alignment of similar carbon-based filler particles such as carbon nanotubes.[16] It can be reasoned that the difference in bulk material conductivity of the 1 wt% rGO composite shown in Figure 4a and the impedance of the 1 wt% microcoil shown in Figure 4b is due to both the DLW printing process imparting non-ideal particle distribution and alignment as well as contributions of contact resistance when probing the microcoil during the impedance analysis.

The ability to successfully create conductive structures directly inside of microfluidic channels has the potential to advance many areas of research and commercial fields. In this work, we presented important first steps that serve as a critical baseline in demonstrating that DLW can be employed to print 3D rGO-laden microstructures inside of microfluidic channels without the need for any thermal post-processing. In Figure 4c we compare the rGO composite in this work to previously developed rGO composites for various other fabrication processes/applications reviewed in a recent article on electrical percolation of graphene-polymer composites.[40] Comparatively, the bulk material's conductivity performance of our composite, though on the lower third of the reviewed data, is comparable to previous works; however, further research remains critical to increase the resulting performance of the structures. Specifically, in future works, the improvement of the composite's electrical performance is an imperative. One of the methods to increase the performance of the DLW-printed microstructures would be to improve the effective filler concentration and dispersion in the composite. Previous works on acrylate-containing photopolymer/carbon-based filler composites have proposed and found success with the use of phenolic/aromatic ring-containing resins as a means to promote π–π stacking and subsequently improving filler dispersions.[16] In contrast to this, IP-Dip is in fact, aliphatic, which passively inhibits rGO dispersion, thereby promoting agglomeration. If a more favorable aromatic polymer is selected, a more efficient, multi-photon polymerization-inducing photoinitiator such as 7-diethylamino-3-thenoylcoumarin (DETC) can be chosen. Photoinitiators such as DETC have been observed to be inducible over a wider range of dosages thereby minimizing the dose accumulation in the 3D DLW-printed structures that causes the burning/bubbling occasionally seen during the printing process as well as driving particle aggregation. Moreover, the development of subsequent graphene-laden photocomposites compatible with multi-photon polymerization, will require the characterization of the contributions of linear and nonlinear absorbances during the fabrication process. The investigation of this absorbance behavior of the composite should ideally include the quantification of the operating laser's pulse intensity after the objective lens, the cross-section and aspect ratio of the material's voxel, and the reflectance of the composite and its filler particles at the operating wavelength and absorption range of the photoinitiator. In addition, with systems that employ high repetition rates such as the Nanoscribe Photonic Professional GT's 80 MHz, it is important to consider thermal contributions as they have been found to play a considerable role in multi-photon polymerization.[41,42] The significance of this work would be further enhanced with the integration of recently developed, DLW-compatible multi-material methods to selectively fabricate structures with both embedded conductive and insulative components.[43] With the implementation of the aforementioned improvements, we believe the utilization of *is*DLW microelectronics in enclosed microfluidic channels will be a pivotal tool in the realization of true integrated 3D sensors. In addition to the mentioned advances in microfabrication, the development of a versatile conductive photocomposite serves to offer the ability to fabricate structures on multiple length scales with minimal alterations due to the similar polymerization chemistries utilized in light-based additive manufacturing strategies such as digital light projection (DLP), stereolithography (SLA), and projection micro stereolithography (PμSL).[9,44]

Experimental Section

Purchased GO (Sigma-Aldrich) containing 15–20 sheets was reduced down to reduced graphene oxide (rGO) through a previously demonstrated reduction scheme[25] in which GO was mixed with a 55% solution of hydroiodic acid (HI) (Sigma-Aldrich) at a concentration of 12.22 mg mL^{-1}. The solution was then stirred at 1500 rpm at 90 °C for 10 h. After the GO was reduced, the solution was centrifuged at 4500 rpm for 1 h, and a subsequent wash in DI and centrifugation was done to remove excess HI. The rGO pellet was resuspended in dimethylformamide (DMF) (Fisher Scientific) to form a 1.1 mg mL^{-1}

solution and passed through a 5 μm nylon syringe filter. After the filtration, the solution was centrifuged again for 1 h at 4500 rpm, the supernatant was removed and subsequently washed with ethanol (Fisher Scientific) before drying overnight under a fume hood.

Cyclic olefin polymer (COP) microfluidic devices were created following the group's previously established protocols.[45] Briefly, a negative master mold was printed via DLW on silicon, which was then hot-embossed for 3 min at 120 °C into a 3 mm COP sheet (ZEONOR 1060R) to form the top of the microfluidic device. Inlet and outlet holes were then drilled into the molded COP. The surface of a 100 μm-thick COP film (microfluidic ChipShop GmbH, Germany) was exposed to vapor-phase cyclohexane (Fisher Scientific) at 30 °C for 2 min. Following this exposure, the COP film and micromolded COP sheet were uniformly pressed and held together for 1 min. To facilitate SEM imaging of *is*DLW-fabricated microstructures, the COP-COP bonding and *is*DLW printing protocols were modified to enable detachment of the COP base. Specifically, the cyclohexane exposure time was reduced to achieve a relatively weak bond between the 100 μm-thick COP film and the micromolded COP sheet.

Samples with a range from 0 to 10% wt rGO content were created by first weighing out the rGO solids and then adding the 1 mL of the photopolymer IP-Dip (Nanoscribe), which was previously warmed to 60 °C to aid in the initial mixing. The slurry was then vortexed for 30 s and left to complete the mixing in an ultrasonic bath (Branson 2800) for 24 h. Following the completion of the mixing, the resist was centrifuged for 30 min at 3000 rpm to remove any substantial aggregates. While not in use, the photocomposite was kept under constant stirring with a magnetic stir plate in a light-proof, glass vial. All 3D architectures fabricated in this work were modeled using Fusion360 (Autodesk) CAD software, exported as STL files, and then imported and sliced in Nanoscribe's proprietary computer-aided manufacturing (CAM) software, DeScribe.

To print graphene-laden microstructures inside of a microfluidic channel using DLW, we adapted the previously reported *is*DLW strategy[13,45] for use with the graphene-laden photocomposite. Initially, this process entailed infusing the liquid-phase graphene-laden photocomposite into a COP microfluidic device (Figure 1a,b), and then loading the device into a Nanoscribe Photonic Professional GT DLW printer with a 63× objective in the oil-immersion configuration (Figure 1c). The printing laser's pulse energy at the objective was calculated to be 0.375 nJ. The printer was then used to selectively polymerize the photocomposite via two-photon (or multi-photon) polymerization. A "ceiling-to-floor" DLW strategy,[13] was employed in which structures were printed at the tallest point of the microchannel first (Figure 1d–g). In this printing configuration, the laser travels through the objective lens, passing through an immersion oil, the thin COP base sheet, and then into the liquid-phase photomaterial to a focal-point, initiating the two-photon polymerization process and subsequently curing the photomaterial. Printing with the "ceiling-to-floor" method was strategically used to prevent the printing laser from having to pass through any previously cured polymer-rGO matrix, thereby reducing the degradation of the laser dosage due to refraction, reflection, and/or absorption caused by the solidified photoresist. When the printing process was initiated, the laser moves in a point-by-point, layer-by-layer manner trapping the rGO particles inside of a polymerized matrix to form a cured, rGO 3D matrix directly inside and fully bonded to the microfluidic channel (Figure 1h). Following the DLW completion, the temporarily bonded COP sheet attached to the bottom of microfluidic device was removed to enhance the imaging of the structures. The remaining top of the device was placed in a bath of propylene glycol monomethyl ether acetate (PGMEA) (Sigma-Aldrich), covered, and left for approximately 45 min followed by isopropyl alcohol (IPA) (Fisher Scientific) for an additional 15 min.

Dynamic light scattering (DLS) testing was carried out on a NanoBrook Omni (Brookhaven Instruments, Holtsville, NY), with a 1 cm quartz cuvette, at 25 °C and $\lambda = 633$ nm. Scattered light was collected at a backscattering angle of 173°. To prepare samples for characterization, rGO or GO were suspended in DMF and diluted to 0.1 mg mL^{-1}. The samples were sonicated for 1 h and then filtered using a 5 μm nylon filter to remove dust and large aggregates. Scanning electron microscopy (SEM) was conducted using a Hitachi SU-70 Schottky field emission gun SEM (Hitachi, Japan) with an accelerating voltage of 5 kV and a 15 mm working distance. Fluorescent imaging was completed using a ZEISS Axio Observer Z1 inverted fluorescence microscope (Oberkochen, Germany). Optical density testing was conducted using a Tescan Spark Multimode microplate reader (Brno, Czech Republic) over a wavelength range of 350 to 800 nm. To prevent over-saturation of the detector, each sample was serially diluted to 100× in DMF and a sample volume of 200 μL was used. Raman spectroscopy was carried out on composite thin films using a LabRAM ARAMIS Raman microscope (Kyoto, Japan). The spectra were acquired using a 633 nm laser in air with a 100× objective under ambient conditions. Multiple spectra were collected at different locations to account for any spatial variability in the samples. Resistivity measurements were conducted on single-photon cured, thin film samples using a Signatone Pro4 four-point resistivity system (Lucas Signatone Corp., Gilroy, CA) equipped with a Kiethley 2600 series (Keithley Instruments, Solon, OH) sourcemeter. Impedance testing was conducted over a frequency range of 1 kHz–2 MHz with an Agilent E4980A (Agilent Technologies, Santa Clara, CA) precision LCR meter at 2 V. A two-probe configuration was employed, and the probe tips were directly placed on the 100 μm × 50 μm × 2 μm contact pads incorporated into the DLW printed microcoil's design. All testing was conducted a minimum of three times to assure accuracy.

Supporting Information

Supporting Information is available from the Wiley Online Library or from the author.

Acknowledgements

The authors greatly appreciate the help and support of the members of the Bioinspired Advanced Manufacturing (BAM) Laboratory as well as the technical staff and members of the Maryland Nanocenter and Terrapin Works. This work was supported in part by U.S. National Science Foundation (NSF) Award Number 1943356, National Center for Manufacturing Science (NCMS) Award Number 130709, U.S. Army Research Laboratory (ARL) Award Number W911NF2020222, and U.S. Army Research Laboratory Cooperative Agreement (CA) W911NF-16-2-0008 administered by Oak Ridge Associated University (ORAU).

Conflict of Interest

The authors declare no conflict of interest.

Data Availability Statement

The data that support the findings of this study are available from the corresponding author upon reasonable request.

Keywords

cyclic olefin polymer, direct laser writing, graphene oxide, reduced graphene oxide

Received: February 23, 2021
Revised: May 1, 2021

[1] A. Koh, D. Kang, Y. Xue, S. Lee, R. M. Pielak, J. Kim, T. Hwang, S. Min, A. Banks, P. Bastien, M. C. Manco, L. Wang, K. R. Ammann, K.-I. Jang, P. Won, S. Han, R. Ghaffari, U. Paik, M. J. Slepian, G. Balooch, Y. Huang, J. A. Rogers, *Sci. Transl. Med.* **2016**, *8*, 366ra165.

[2] A. Gumennik, A. M. Stolyarov, B. R. Schell, C. Hou, G. Lestoquoy, F. Sorin, W. McDaniel, A. Rose, J. D. Joannopoulos, Y. Fink, *Adv. Mater.* **2012**, *24*, 6005.

[3] H. Y. Y. Nyein, M. Bariya, L. Kivimäki, S. Uusitalo, T. S. Liaw, E. Jansson, C. H. Ahn, J. A. Hangasky, J. Zhao, Y. Lin, T. Happonen, M. Chao, C. Liedert, Y. Zhao, L.-C. Tai, J. Hiltunen, A. Javey, *Sci. Adv.* **2019**, *5*, eaaw9906.

[4] Q. Wang, A.-A. D. Jones, J. A. Gralnick, L. Lin, C. R. Buie, *Sci. Adv.* **2019**, *5*, eaat5664.

[5] R. Ahmed, M. O. Ozen, M. G. Karaaslan, C. A. Prator, C. Thanh, S. Kumar, L. Torres, N. Iyer, S. Munter, S. Southern, T. J. Henrich, F. Inci, U. Demirci, *Adv. Mater.* **2020**, *32*, 1907160.

[6] J. Smits, J. T. Damron, P. Kehayias, A. F. McDowell, N. Mosavian, I. Fescenko, N. Ristoff, A. Laraoui, A. Jarmola, V. M. Acosta, *Sci. Adv.* **2019**, *5*, eaaw7895.

[7] W. Yu, H. Lin, Y. Wang, X. He, N. Chen, K. Sun, D. Lo, B. Cheng, C. Yeung, J. Tan, D. Di Carlo, S. Emaminejad, *Sci. Robot.* **2020**, *5*, eaba4411.

[8] K. Mutafopulos, P. Spink, C. D. Lofstrom, P. J. Lu, H. Lu, J. C. Sharpe, T. Franke, D. A. Weitz, *Lab Chip* **2019**, *19*, 2435.

[9] R. D. Sochol, E. Sweet, C. C. Glick, S.-Y. Wu, C. Yang, M. Restaino, L. Lin, *Microelectron. Eng.* **2018**, *189*, 52.

[10] H. T. Le, I. Mizushima, Y. Nour, P. T. Tang, A. Knott, Z. Ouyang, F. Jensen, A. Han, *Microsyst. Nanoeng.* **2018**, *4*, 17082.

[11] N. Zhou, C. Liu, J. A. Lewis, D. Ham, *Adv. Mater.* **2017**, *29*, 1605198.

[12] M. R. Gullo, S. Takeuchi, O. Paul, *Adv. Healthcare Mater.* **2017**, *6*, 1601053.

[13] A. C. Lamont, A. T. Alsharhan, R. D. Sochol, *Sci. Rep.* **2019**, *9*, 394.

[14] T. Bückmann, N. Stenger, M. Kadic, J. Kaschke, A. Frölich, T. Kennerknecht, C. Eberl, M. Thiel, M. Wegener, *Adv. Mater.* **2012**, *24*, 2710.

[15] F. Mayer, S. Richter, J. Westhauser, E. Blasco, C. Barner-Kowollik, M. Wegener, *Sci. Adv.* **2019**, *5*, eaau9160.

[16] S. Ushiba, S. Shoji, K. Masui, J. Kono, S. Kawata, *Adv. Mater.* **2014**, *26*, 5653.

[17] A. Vyatskikh, S. Delalande, A. Kudo, X. Zhang, C. M. Portela, J. R. Greer, *Nat. Commun.* **2018**, *9*, 593.

[18] S. Kang, K. Vora, E. Mazur, *Nanotechnology* **2015**, *26*, 121001.

[19] Y. Liu, W. Xiong, D. W. Li, Y. Lu, X. Huang, H. Liu, L. S. Fan, L. Jiang, J.-F. Silvain, Y. F. Lu, *Int. J. Extreme Manuf.* **2019**, *1*, 025001.

[20] Q. Hu, X.-Z. Sun, C. D. J. Parmenter, M. W. Fay, E. F. Smith, G. A. Rance, Y. He, F. Zhang, Y. Liu, D. Irvine, C. Tuck, R. Hague, R. Wildman, *Sci. Rep.* **2017**, *7*.

[21] E. Blasco, J. Müller, P. Müller, V. Trouillet, M. Schön, T. Scherer, C. Barner-Kowollik, M. Wegener, *Adv. Mater.* **2016**, *28*, 3592.

[22] W. Xiong, Y. Liu, L. J. Jiang, Y. S. Zhou, D. W. Li, L. Jiang, J.-F. Silvain, Y. F. Lu, *Adv. Mater.* **2016**, *28*, 2002.

[23] I. Cooperstein, E. Sachyani-Keneth, E. Shukrun-Farrell, T. Rosental, X. Wang, A. Kamyshny, S. Magdassi, *Adv. Mater. Interfaces* **2018**, *5*, 1800996.

[24] C. Tan, X. Cao, X.-J. Wu, Q. He, J. Yang, X. Zhang, J. Chen, W. Zhao, S. Han, G.-H. Nam, M. Sindoro, H. Zhang, *Chem. Rev.* **2017**, *117*, 6225.

[25] I. M. Leo, E. Soto, F. Vaquero, N. Mota, B. Garcia, D. Liuzzi, R. Guil-López, R. M. Navarro, J. L. G. Fierro, *Top. Catal.* **2017**, *60*, 1183.

[26] I. A. Kinloch, J. Suhr, J. Lou, R. J. Young, P. M. Ajayan, *Science* **2018**, *362*, 547.

[27] Y. Xu, M. J. Pospisil, M. J. Green, *Nanotechnology* **2016**, *27*, 235702.

[28] D. Tristant, P. Puech, I. C. Gerber, *Phys. Chem. Chem. Phys.* **2015**, *17*, 30045.

[29] H.-J. Choi, M. S. Kim, D. Ahn, S. Y. Yeo, S. Lee, *Sci. Rep.* **2019**, *9*, 6338.

[30] J. R. Potts, O. Shankar, L. Du, R. S. Ruoff, *Macromolecules* **2012**, *45*, 6045.

[31] Z. Samir, Y. El Merabet, M. P. F. Graça, S. S. Teixeira, M. E. Achour, L. C. Costa, *Polym. Compos.* **2018**, *39*, 1297.

[32] S. C. C. Shih, I. Barbulovic-Nad, X. Yang, R. Fobel, A. R. Wheeler, *Biosens. Bioelectron.* **2013**, *42*, 314.

[33] J. Rho, W. Jang, I. Hwang, D. Lee, C. H. Lee, T. D. Chung, *Biosens. Bioelectron.* **2018**, *102*, 121.

[34] I. Ciani, H. Schulze, D. K. Corrigan, G. Henihan, G. Giraud, J. G. Terry, A. J. Walton, R. Pethig, P. Ghazal, J. Crain, C. J. Campbell, T. T. Bachmann, A. R. Mount, *Biosens. Bioelectron.* **2012**, *31*, 413.

[35] K. Madgula, L. N. Shubha, in *Functional Nanomaterials*, (Eds.: S. Thomas, N. Joshi, V. K. Tomer), Springer Singapore, Singapore **2020**, pp. 399–431.

[36] J. Terrones, J. A. Elliott, J. J. Vilatela, A. H. Windle, *ACS Nano* **2014**, *8*, 8497.

[37] E. L. Papadopoulou, F. Pignatelli, S. Marras, L. Marini, A. Davis, A. Athanassiou, I. S. Bayer, *RSC Adv.* **2016**, *6*, 6823.

[38] A. Oskouyi, U. Sundararaj, P. Mertiny, *Nanoscale Res. Lett.* **2014**, *9*, 369.

[39] J. Vaithilingam, P. Sanjuan-Alberte, S. Campora, G. A. Rance, L. Jiang, J. Thorpe, L. Burroughs, C. J. Tuck, C. Denning, R. D. Wildman, R. J. M. Hague, M. R. Alexander, F. J. Rawson, *Adv. Funct. Mater.* **2019**, *29*, 1902016.

[40] A. J. Marsden, D. G. Papageorgiou, C. Vallés, A. Liscio, V. Palermo, M. A. Bissett, R. J. Young, I. A. Kinloch, *2D Mater.* **2018**, *5*, 032003.

[41] M. Malinauskas, A. Žukauskas, G. Bičkauskaitė, R. Gadonas, S. Juodkazis, *Opt. Express* **2010**, *18*, 10209.

[42] J. B. Mueller, J. Fischer, Y. J. Mange, T. Nann, M. Wegener, *Appl. Phys. Lett.* **2013**, *103*, 123107.

[43] A. C. Lamont, M. A. Restaino, M. J. Kim, R. D. Sochol, *Lab Chip* **2019**, *19*, 2340.

[44] Q. Ge, Z. Li, Z. Wang, K. Kowsari, W. Zhang, X. He, J. Zhou, N. X. Fang, *Int. J. Extreme Manuf.* **2020**, *2*, 022004.

[45] A. T. Alsharhan, R. Acevedo, R. Warren, R. D. Sochol, *Lab Chip* **2019**, *19*, 2799.